

# Inferring the internal structure of $\gamma$ Doradus variables from Rossby modes

## Extension of the $\nu - \sqrt{\Delta\nu}$ diagram

M. Takata<sup>1</sup>, R.-M. Ouazzani<sup>2</sup>, H. Saio<sup>3</sup>, S. Christophe<sup>2</sup>, J. Ballot<sup>4</sup>, V. Antoci<sup>5,6</sup>, and S. J. A. J. Salmon<sup>7</sup>

<sup>1</sup> Department of Astronomy, School of Science, The University of Tokyo, 7-3-1 Hongo, Bunkyo-ku, Tokyo 113-0033, Japan  
e-mail: [takata@astron.s.u-tokyo.ac.jp](mailto:takata@astron.s.u-tokyo.ac.jp)

<sup>2</sup> LESIA, Observatoire de Paris, PSL Research University, CNRS, Sorbonne Universités, UPMC Univ. Paris 06, Univ. Paris Diderot, Sorbonne Paris Cité, 5 place Jules Janssen, 92195 Meudon, France

<sup>3</sup> Astronomical Institute, Graduate School of Science, Tohoku University, Sendai 980-8578, Japan

<sup>4</sup> IRAP, Université de Toulouse, CNRS, UPS, CNES, 14 avenue Édouard Belin, 31400 Toulouse, France

<sup>5</sup> DTU Space, National Space Institute, Technical University of Denmark, Elektrovej 328, 2800 Kgs. Lyngby, Denmark

<sup>6</sup> Stellar Astrophysics Centre, Department of Physics and Astronomy, Aarhus University, Ny Munkegade 120, 8000 Aarhus C, Denmark

<sup>7</sup> Observatoire de Genève, Université de Genève, 51 Ch. Des Maillettes, 1290 Sauverny, Switzerland

Received 6 April 2020 / Accepted 9 October 2020

### ABSTRACT

A unique type of oscillation modes has recently been identified in  $\gamma$  Doradus variables. These low-frequency modes are called Rossby modes (or  $r$  modes) because they consist of Rossby waves in each spherical layer. These waves are characterised by toroidal motions that are restored by the latitudinal variation in the Coriolis force. The horizontal oscillations are weakly coupled in the radial direction. We show that these modes can be used to probe the interior of the stars. The method of the  $\nu - \sqrt{\Delta\nu}$  diagram, which has originally been developed to analyse another type of modes, Kelvin  $g$ -modes (or prograde sectoral  $g$ -modes), is extended to take Rossby modes into account. We first show based on a theoretical model and then on two stars, KIC 3240967 and KIC 12066947, that the method can be adapted to Rossby modes straightforwardly. In addition, we demonstrate that simultaneous analysis of Kelvin and Rossby modes results in (1) smaller uncertainties in the internal rotation rate and the characteristic period of gravity modes, and (2) a substantial reduction of the correlation between the estimates of the two parameters.

**Key words.** asteroseismology – stars: oscillations – stars: rotation – methods: data analysis

## 1. Introduction

Recent space missions for exoplanet study, such as CoRoT<sup>1</sup> (Baglin et al. 2006), *Kepler* (Borucki et al. 2010), and TESS<sup>2</sup> (Ricker et al. 2014), have brought (and still bring) dramatic changes in asteroseismology, the study of the interior of stars based on their oscillation. The change can be considered to be twofold from an observational point of view. On the one hand, high-precision photometric data have unambiguously revealed oscillations with tiny amplitudes. Typical examples include solar-like oscillations in a large number of main-sequence and evolved stars (e.g. Chaplin & Miglio 2013). On the other hand, long-term continuous observations have clearly resolved complicated spectra of oscillation frequencies. One of the most successful cases is found in  $\gamma$  Doradus ( $\gamma$  Dor) stars (e.g. Van Reeth et al. 2015). This is a class of intermediate-mass main-sequence oscillators. They benefit from continuous observations from space because they have many oscillation periods of the order of one day, which show serious aliasing problems when they are observed from ground.

The observations from space have also strongly affected theoretical studies. Before the space age, when the data quality was poor, studies of stellar oscillations were often motivated by theoretical interest. Some oscillation modes of special physical characters have been discussed without regard to whether they are detected in real stars. Two examples can be listed here: mixed modes in evolved stars (Osaki 1975), and Rossby modes (or  $r$ -modes) in rotating stars (Papaloizou & Pringle 1978). The space missions did indeed detect both of these modes (Bedding et al. 2010; Beck et al. 2011; Van Reeth et al. 2016; Saio et al. 2018), which stimulates fresh theoretical interests to establish asteroseismology. Mixed modes have a dual character of acoustic and gravity modes because they consist of internal gravity waves in the dense central core and acoustic waves in the extended envelope. They play a major role in red giant seismology (e.g. Bedding et al. 2011; Mosser et al. 2011; Beck et al. 2012). Rossby modes can be regarded as global counterparts of Rossby waves, which are known from meteorology (Rossby 1939; Gill 1982). The phase of these waves propagates in the opposite direction to the rotation in the co-rotating frame, showing toroidal motions in each spherical layer of stars. The horizontal propagation can be understood based on the conservation of the potential vorticity. The latitudinal variation in the Coriolis force serves as the restoring force. These modes are the

<sup>1</sup> CoRoT is an abbreviation of Convection, Rotation and planetary Transits.

<sup>2</sup> TESS stands for the Transiting Exoplanet Survey Satellite.

second most common modes in  $\gamma$  Dor stars after Kelvin  $g$ -modes (or prograde sectoral  $g$ -modes), which are global manifestations of equatorial Kelvin waves (Thomson 1880; Gill 1982). The two types of modes can explain most of the detected modes (e.g. Li et al. 2020). The dominance of these modes, particularly in rapid rotators, can probably be understood by the smaller geometrical cancellation of photometric signals over the visible hemisphere than the other types of modes, but the weaker radiative damping caused by the longer horizontal wavelengths could also contribute. It has been claimed that Rossby modes are also found in other types of stars (Saio 2018).

The oscillation periods of  $\gamma$  Dor stars are much longer than the dynamical timescale at the surface of about an hour, while their rotation has periods of the same order as the oscillation. Because oscillations like this are thought to be strongly affected by rotation, they provide us with an ideal opportunity to study the internal rotation and structure of these stars. Takata et al. (2020) (hereafter, Paper I) developed a method for extracting the following two parameters from the frequencies of Kelvin  $g$ -modes: the (average) rotation frequency  $\nu_{\text{rot}}$  and the characteristic period  $P_0$  of gravity-mode oscillations. We note that  $P_0$  can be regarded as a measure of the evolutionary stage because it monotonically decreases with stellar evolution. The main purpose of the paper is to revise the method so that Rossby modes are included.

Helioseismology has shown that it is important to consider multiple types of modes to infer the stellar structure accurately (e.g. Gough 1985) because different types of modes represent different aspects of the structure. It is essential to use acoustic modes in a wide range of spherical degrees that have different inner turning points to constrain the profile of the sound speed from the near-surface layers to the deep interior of the Sun. The detection of only a few gravity modes in addition to a large number of acoustic modes is expected to significantly improve the inversion results of the rotation and the sound speed near the centre. Similarly, the rotation rates of the core and envelope of evolved stars have been estimated from mixed modes with various degrees of mixture of acoustic and gravity modes (e.g. Deheuvels et al. 2012, 2014). In the case of (slowly rotating) main-sequence hybrid pulsators of  $\delta$  Sct and  $\gamma$  Dor type, the rotation rates have been determined independently in the envelope and the core from acoustic and gravity modes, respectively (Kurtz et al. 2014; Saio et al. 2015; Schmid et al. 2015). The inferred contrasts in the rotation rates between the core and the envelope give valuable information about the problem of angular momentum transport inside stars. We discuss whether a similar improvement can be observed in the seismic inferences of  $\gamma$  Dor stars by combining Rossby modes with Kelvin  $g$ -modes.

The structure of the paper is as follows: we extend in Sect. 2 the method of the  $\nu - \sqrt{\Delta\nu}$  diagram to take not only Kelvin  $g$ -modes into account, but Rossby modes as well. The extended method is validated based on a theoretical model in Sect. 3. The method is applied to real stars in Sect. 4. Section 5 is devoted to the discussion and conclusion.

## 2. Method

The fundamental formula of our analysis is the asymptotic expression of the oscillation frequencies in the traditional approximation of rotation (Eckart 1960). This is generally known to be a good approximation for low-frequency oscillations in rotating stars, which consist of waves with short wavelengths in the radial direction (e.g. Ballot et al. 2012; Ouazzani et al. 2017). The details are described in Paper I, therefore we only

give a concise description of the framework here. The period in the co-rotating frame is provided by

$$\nu_{\text{co}}^{-1} = \frac{(|n| + \alpha) P_0}{\sqrt{\lambda}}, \quad (1)$$

in which the meanings of the symbols are given as follows:  $\nu_{\text{co}}$  is the oscillation frequency in the co-rotating frame,  $n$  is the radial order of oscillation modes ( $n < 0$  and  $|n| \gg 1$ ),  $\alpha$  is the phase changes introduced at the inner and outer boundaries of the propagation region,  $P_0$  is the characteristic period of the gravity modes, and  $\lambda$  is the eigenvalue of the Laplace tidal equation. If the rotation frequency  $\nu_{\text{rot}}$  is not constant but weakly dependent on the distance from the centre,  $r$ , the co-rotating frame should be interpreted as the frame that rotates with the weighted average over the propagation region (G),

$$\langle \nu_{\text{rot}} \rangle = \frac{\int_G \frac{N(r)}{r} \nu_{\text{rot}}(r) dr}{\int_G \frac{N(r)}{r} dr}, \quad (2)$$

where  $N$  is the Brunt–Väisälä frequency. We do not consider the case of strong differential rotation in this paper. The definition of  $P_0$  is given by

$$P_0 = 2\pi^2 \left( \int_G \frac{N(r)}{r} dr \right)^{-1}. \quad (3)$$

In the limit of no rotation, the frequencies of high-order  $g$ -modes with spherical degree  $\ell$  are evenly spaced in period with  $P_0 / \sqrt{\ell(\ell+1)}$ . We adopt the conventions that  $\nu_{\text{rot}}$ ,  $\nu_{\text{co}}$ , and the oscillation frequency in the inertial frame,  $\nu$ , are all positive, and that the azimuthal order  $m$  is positive (negative) for prograde (retrograde) modes. These quantities are related to each other by

$$\nu = |\nu_{\text{co}} + m\nu_{\text{rot}}|. \quad (4)$$

We developed in Paper I the method of the  $\nu - \sqrt{\Delta\nu}$  diagram, in which  $\Delta\nu$  means the difference between the two adjacent frequencies, to estimate  $\nu_{\text{rot}}$  and  $P_0$  from the observed frequencies of Kelvin  $g$ -modes. Its main point is to reduce the problem of non-linear fitting to that of iterative linear fitting, which is easier to understand and far easier to solve. This reduction is made possible because  $\lambda$  of Kelvin  $g$ -modes with a given  $m$  is nearly independent of the spin parameter, which is defined by

$$s = \frac{2\nu_{\text{rot}}}{\nu_{\text{co}}}. \quad (5)$$

We observe in Fig. 1 that

$$\sqrt{\lambda} \approx |m| \quad \text{as } s \rightarrow \infty \text{ for Kelvin } g\text{-modes.} \quad (6)$$

Rossby modes share a similar property because

$$\sqrt{\lambda} \approx \frac{|m|}{2|k|-1} \quad \text{as } s \rightarrow \infty \text{ for Rossby modes with } k \leq -2 \quad (7)$$

(cf. Townsend 2003). We note that the index  $k$  is related to the structure of the corresponding eigenfunction (Hough function) of the Laplace tidal equation (cf. Lee & Saio 1997) such that for retrograde modes with  $k \leq -1$ , the number of nodes is equal to  $|k|$  and  $|k+2|$  for odd and even  $|k|$ , respectively. In particular, the Hough function associated with an even (odd) value of  $|k|$  is symmetric (anti-symmetric) with respect to the equator.

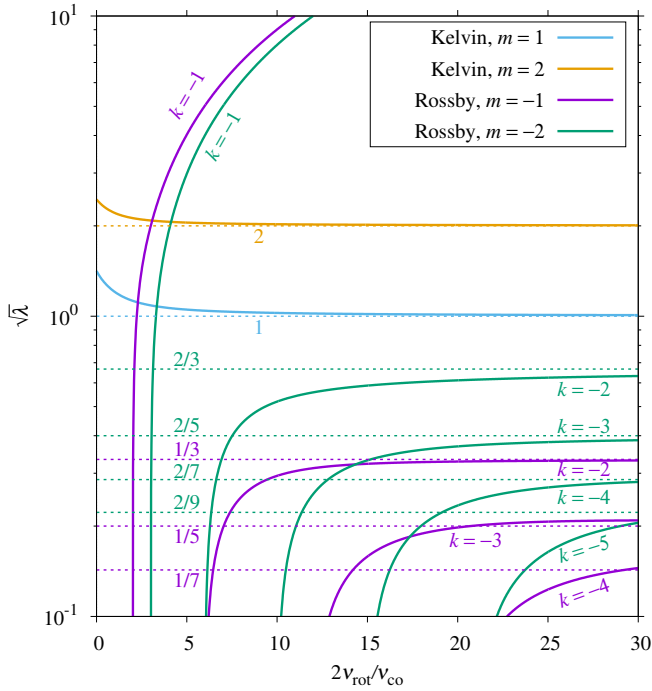


**Fig. 1.** Profiles of  $\sqrt{\lambda}$  of Kelvin  $g$ -modes with  $m = 1, 2$  and Rossby modes with  $m = -1, -2$ . The asymptotic values as  $2\nu_{\text{rot}}/\nu_{\text{co}} \rightarrow \infty$  are indicated by the horizontal dotted lines.

We may therefore construct the  $\nu - \sqrt{\Delta\nu}$  diagram for these Rossby modes in just the same way as Kelvin  $g$ -modes in Paper I. If a list of frequency  $\{\nu_i\}$  with the same  $m$  and  $k$  is given in ascending order, we can derive the approximate relation,

$$-\frac{1}{\sqrt{2|k|-1}} \sqrt{\frac{\Delta_i \nu}{|m| \Delta_i n}} \approx \sqrt{P_0} \left( \frac{\nu_{i+\frac{1}{2}}}{|m|} - \nu_{\text{rot}} \right), \quad (8)$$

for  $|n| \gg 1$  or  $s \gg 1$ . Here we have introduced  $\Delta_i \nu = \nu_{i+1} - \nu_i$ ,  $\Delta_i n = |n_{i+1} - n_i|$ , and  $\nu_{i+\frac{1}{2}} = (\nu_i + \nu_{i+1})/2$ , in which  $n_i$  stands for the radial order of the mode with the  $i$ -th frequency. Equation (8) means that there is a linear relation between  $\nu_{i+\frac{1}{2}}$  and  $\sqrt{\Delta_i \nu / \Delta_i n}$ . This is different from the corresponding relation for Kelvin  $g$ -modes (Eq. (10) of Paper I) only in the first factor on the left-hand side,  $-1/\sqrt{2|k|-1}$ , which is missing in the latter. The negative sign on the left-hand side arises because the frequency difference of two adjacent Rossby modes is smaller for higher frequencies, which is opposite to the case of Kelvin  $g$ -modes. The right-hand side is accordingly negative. This is because of  $\nu_{\text{co}} < \nu_{\text{rot}}$  for Rossby modes (e.g. Saio et al. 2018) and Eq. (4), which is reduced to

$$\nu - |m| \nu_{\text{rot}} = -\nu_{\text{co}} < 0. \quad (9)$$

While the linear relation given by Eq. (8) is valid only for Rossby modes in the limit of  $s \gg 1$ , we choose to use the more general non-linear relation in this analysis (cf. Eq. (10)).

As in the case of Kelvin  $g$ -modes in Paper I, we may generalise Eq. (8) to take the Kelvin and Rossby modes into account as

$$y_i = \sqrt{P_0} (x_i - \nu_{\text{rot}}), \quad (10)$$

in which  $x_i$  and  $y_i$  are defined by

$$x_i = \frac{\nu_{i+\frac{1}{2}}}{|m|} \quad (11)$$

and

$$y_i = f_i(\nu_{\text{rot}}) \sqrt{\frac{\Delta_i \nu}{|m| \Delta_i n}}, \quad (12)$$

respectively. We have introduced  $f_i$  in Eq. (12), which is given by

$$f_i(\nu_{\text{rot}}) = \left[ \frac{-1}{|m| \Delta_i \nu} \Delta_i \left( \frac{\sqrt{\lambda}}{\nu_{\text{co}}} \right) \right]^{\frac{1}{2}} \left( \nu_{i+\frac{1}{2}} - |m| \nu_{\text{rot}} \right), \quad (13)$$

to consider the deviations from the asymptotic expressions of  $\sqrt{\lambda}$  (Eqs. (6) and (7)) and those from the linearisation relation,  $\Delta_i \nu^{-1} \approx -\nu^{-2} \Delta_i \nu$ . Because  $f_i$  depends on  $\nu_{\text{rot}}$  and the frequency of each mode, Eq. (10) is a non-linear equation. As  $\nu_{\text{rot}} \rightarrow \infty$ ,  $f_i(\nu_{\text{rot}})$  is asymptotically equal to

$$f_i(\nu_{\text{rot}}) \approx f_0 = \begin{cases} 1 & \text{for Kelvin } g\text{-modes,} \\ -\frac{1}{\sqrt{2|k|-1}} & \text{for Rossby modes with } k \leq -2. \end{cases} \quad (14)$$

When we correctly identify  $m$ ,  $k$ , and  $\Delta_i n$ , we can develop the procedure of iterative linear fitting to estimate  $\nu_{\text{rot}}$  and  $P_0$  from the frequency list  $\{\nu_i\}$  based on Eq. (10) (cf. Paper I). The initial values of  $f_i$  can be set to  $f_0$  independent of  $i$  (and hence frequency). We stress, however, that  $f_i(\nu_{\text{rot}})$  is updated with a new value of  $\nu_{\text{rot}}$  after each iteration based on Eq. (13), which depends on  $\nu_i$  and  $\nu_{i+1}$ . The uncertainties in the estimated parameters can be evaluated with the method described in Appendix A of Paper I. We note that these uncertainties should be considered as formal because the systematic errors in Eq. (10) are not taken into account.

Figure 1 shows that the case of  $k = -1$  is exceptional because  $\sqrt{\lambda}$  does not tend to any constant, but

$$\sqrt{\lambda} \approx s - |m| \quad \text{as } s \rightarrow \infty \text{ for Rossby modes with } k = -1. \quad (15)$$

These were called retrograde Yanai modes by Townsend (2003), and are composed of more gravity waves than Rossby waves when the rotation is rapid ( $s \gg 1$ ). Because these modes are rarely detected and resolved even in the *Kepler* data (cf. Saio et al. 2018; Li et al. 2020), we do not consider them to estimate  $\nu_{\text{rot}}$  and  $P_0$ .

### 3. Tests based on an evolutionary model

We applied the method of the  $\nu - \sqrt{\Delta\nu}$  diagram to a typical theoretical model of  $\gamma$  Dor stars. The model is the same as Model A of Christophe et al. (2018) and Paper I, which has a mass of  $1.86 M_{\odot}$  and  $\nu_{\text{rot}} = 7 \mu\text{Hz}$ . We first used the frequencies of Rossby modes alone, and then used those of both Kelvin and Rossby modes.

#### 3.1. Analysis based on Rossby modes alone

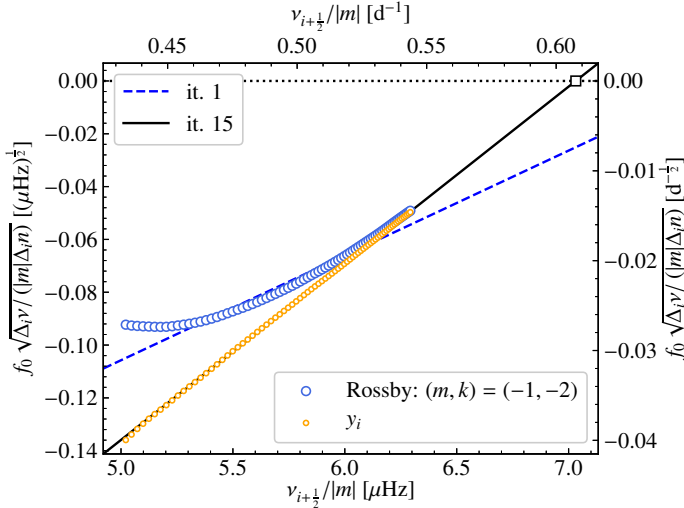
The frequencies of Rossby modes were computed with the ACOR oscillation code (Ouazzani et al. 2012, 2015) for  $m = -1$ ,  $k = -2$  and the radial order from  $n = -21$  to  $-99$ . The corresponding range of the spin parameter is roughly between  $s = 7$  and 20. The  $\nu - \sqrt{\Delta\nu}$  diagram is shown in Fig. 2, and the estimates for  $\nu_{\text{rot}}$  and  $P_0$  are given in rows 4 and 5 of Table 1.

Figure 2 shows that the open blue circles are not aligned on a straight line, but rather on a concave curve. This is because

**Table 1.** Estimates of  $\nu_{\text{rot}}$  and  $P_0$  for the evolutionary model of a  $\gamma$  Dor star (Model A of Christophe et al. 2018).

	$\nu_{\text{rot}}$ [ $\mu\text{Hz}$ ]	$\nu_{\text{rot}}$ [ $\text{d}^{-1}$ ]	$P_0$ [ $10^3$ s]	$a$	$f_i/f_0$	
					Kelvin	Rossby
Rossby modes with $m = -1$ and $k = -2$						
It. 1	7.66	0.662	1.57			
It. 15	7.032(2)	0.6076(2)	4.47(1)	−0.99		1.01–1.47
Kelvin $g$ -modes with $m = 1$						
It. 1	6.64	0.574	4.03			
It. 5	6.944(8)	0.6000(7)	4.49(1)	0.99	1.002–1.036	
Kelvin and Rossby modes						
It. 1	6.91	0.597	4.31			
It. 6	7.015(2)	0.6061(1)	4.565(3)	0.27	1.002–1.035	1.01–1.46
True value	7	0.605	4.579			

**Notes.** The numbers in the parentheses indicate the formal uncertainties in the last digit of each estimate, which correspond to the 99% confidence intervals. Correlation coefficients  $a$  between the estimates of  $\nu_{\text{rot}}$  and  $P_0$  are given in the fifth column. The range of  $f_i/f_0$  is given for the converged value of  $\nu_{\text{rot}}$  in the sixth and seventh column for Kelvin and Rossby modes, respectively. The results of Paper I are reproduced in the seventh and eighth row.



**Fig. 2.** Diagram of  $\nu$  vs.  $\sqrt{\Delta\nu}$  based on Rossby modes of Model A with  $\nu_{\text{rot}} = 7 \mu\text{Hz}$ . Each mode corresponds to an open blue circle, and the dashed and solid lines indicate the fitted lines of the first and fifteenth iteration, respectively. The open square at the abscissa intercept represents the converged value of  $\nu_{\text{rot}}$ . Small open orange circles indicate the corrected values  $y_i = f_i \sqrt{\Delta\nu} / (|m| \Delta\nu)$  that are calculated for the converged value of  $\nu_{\text{rot}}$ .

the asymptotic relations of Eqs. (7) and (8) for  $m = -1$  and  $k = -2$  are inaccurate particularly for  $s \lesssim 10$ , as Fig. 1 shows. As a result, the fitted line of iteration 1 (the dashed blue line) gives  $\nu_{\text{rot}} = 7.66 \mu\text{Hz}$  and  $P_0 = 1.57 \times 10^3$  s, which are different from the true values by 9% and -66%, respectively. Although the first iteration provides such poor results, the procedure converges after 15 iterations when the relative differences in the estimated  $\nu_{\text{rot}}$  and  $P_0$  between two successive iterations become less than  $10^{-4}$ . We note that  $s$  is smaller for lower frequency modes in Fig. 2, and the deviation of  $f_i(\nu_{\text{rot}})$  from  $f_0$  is accordingly larger. For the converged estimate of  $\nu_{\text{rot}}$ , the correction factor  $f_i/f_0$  is equal to 1.47 for the lowest frequency pair, and it monotonically decreases until it reaches 1.01 for the highest frequency pair. The corrected values  $y_i$  for the converged estimate of  $\nu_{\text{rot}}$  are shown in Fig. 2 as small open orange circles, which are almost perfectly aligned with the fitted (solid) line. We thus

obtain  $\nu_{\text{rot}} = 7.032 \pm 0.002 \mu\text{Hz}$  and  $P_0 = (4.47 \pm 0.01) \times 10^3$  s, which agree with the true values within 0.5% and 2%, respectively. We note that these differences from the true values are larger than the estimated formal uncertainties, which are 0.03% and 0.3% for  $\nu_{\text{rot}}$  and  $P_0$ , respectively. The correlation coefficient  $a$  (cf. Eq. (A.29) of Paper I) between the estimates of  $\nu_{\text{rot}}$  and  $P_0$  is nearly equal to -1. This high anti-correlation can be understood from Fig. 2. All of the open circles are distributed in the lower left side of the abscissa intercept (open square) of the best-fit line (solid line). When the intercept ( $\nu_{\text{rot}}$ ) is slightly moved to the right side and the fitting process is repeated under this condition, the fitted line should have a shallower slope ( $\sqrt{P_0}$ ) because the line must roughly go through the centre of distribution of the open circles. Thus, the increase in  $\nu_{\text{rot}}$  must result in the decrease in  $P_0$ .

In order to determine how robust the iterative procedure is, we performed experiments by discarding high-frequency components in the list step by step. When we used only frequencies below  $5.9 \mu\text{Hz}$ , which corresponds to  $s < 12.5$ , the procedure still converged after 78 iterations. The converged values of  $\nu_{\text{rot}}$  and  $P_0$  are  $7.020 \pm 0.002 \mu\text{Hz}$  ( $0.6066 \pm 0.0002 \text{ d}^{-1}$ ) and  $(4.52 \pm 0.01) \times 10^3$  s, respectively. These are marginally closer to the true values in the last row of Table 1 than the values in row 5 of Table 1, which were obtained by taking all the frequencies into account. The reason for these differences is that the accuracy of Eq. (1) depends on the frequency range. In other words, treatment beyond the traditional approximation of rotation in the asymptotic regime is necessary to discuss this problem further (cf. Sect. 5). On the other hand, the procedure fails to converge even after 100 iterations when the upper limit is set at  $5.8 \mu\text{Hz}$ , which implies  $s < 11.5$ . It is thus essential to include high frequencies in the analysis when Rossby modes alone are used. We confirmed that the procedure without Rossby modes above  $5.8 \mu\text{Hz}$  converges successfully again when we take Kelvin  $g$ -modes into account (cf. Sect. 3.2).

We reproduce the results of Paper I based on Kelvin  $g$ -modes in rows 7 and 8 of Table 1. Comparing these with the case of Rossby modes, we find the following: (a) the number of iteration required for convergence is much larger for Rossby modes (15) than Kelvin modes (5), (b) the converged value of  $\nu_{\text{rot}}$  is higher (lower) by less than 1% than the true value for Rossby (Kelvin) modes, (c) those of  $P_0$  are shorter by 2% than the true



value for both types of modes, and (d) the estimates of  $\nu_{\text{rot}}$  and  $P_0$  are highly anti-correlated (correlated) with each other for Rossby (Kelvin) modes. Point (a) is because the deviation from the asymptotic relation of  $\sqrt{\lambda}$  (cf. Eqs. (6) and (7)) for low values of the spin parameter is more significant for Rossby modes than for Kelvin modes, as shown in Fig. 1. The range of  $f_i/f_0$  is 1.002–1.036 for Kelvin  $g$ -modes, and it is 1.01–1.47 for Rossby modes.

### 3.2. Analysis based on both Kelvin and Rossby modes

In rows 10 and 11 of Table 1 we provide the results based on both Kelvin and Rossby modes. The corresponding  $\nu - \sqrt{\Delta\nu}$  diagram is depicted in Fig. 3. The points we find can be summarised as follows:

1. The differences in the converged values of  $\nu_{\text{rot}}$  and  $P_0$  from the true values are reduced to 0.2% and 0.3%, respectively.
2. The number of iterations required for convergence (6) is much smaller than in the case of Rossby modes (15), and it is similar to the case of Kelvin modes (5).
3. The formal uncertainty of 0.3% in the estimate of  $\nu_{\text{rot}}$  is similar to the case of Rossby modes, and smaller by several factors than in the case of Kelvin modes. The uncertainty of 0.07% for  $P_0$  is smaller by a few factors than in the separate analyses of Rossby and Kelvin modes.
4. Even the outputs of the first iteration ( $\nu_{\text{rot}} = 6.91 \mu\text{Hz}$  and  $P_0 = 4.31 \times 10^3 \text{ s}$ ) give reasonably good estimates of the true values ( $\nu_{\text{rot}} = 7 \mu\text{Hz}$  and  $P_0 = 4.579 \times 10^3 \text{ s}$ ). This can be understood as (partial) cancellation. When Rossby (or Kelvin) modes alone are analysed separately, the first iteration gives larger (or smaller)  $\nu_{\text{rot}}$  and smaller (or larger)  $P_0$  than the true values. These opposite differences come from the behaviour of  $\sqrt{\lambda}$ : it increasingly (decreasingly) approaches the asymptotic value given by Eq. (7) (Eq. (6)) for Rossby (Kelvin) modes, as shown in Fig. 1.
5. The low correlation coefficient of 0.27 between the estimates of  $\nu_{\text{rot}}$  and  $P_0$  indicates the significant improvement from the cases that use Rossby or Kelvin modes alone. While the estimates are highly anti-correlated for Rossby modes (cf. Sect. 3.1), they are highly correlated for Kelvin modes because Kelvin modes are distributed in the upper right side of the abscissa intercept, as discussed in Paper I. The simultaneous analysis of Rossby and Kelvin modes demonstrates that it is essential to have points on either side of the abscissa intercept in the  $\nu - \sqrt{\Delta\nu}$  diagram to decrease the (anti-) correlation between the estimates of  $\nu_{\text{rot}}$  and  $P_0$ .

## 4. Application to real stars

### 4.1. KIC 3240967

We first studied a  $\gamma$  Dor star, KIC 3240967, which shows a clear series of Rossby modes as well as Kelvin  $g$ -modes (cf. Li et al. 2019). The amplitude spectrum (Lomb-Scargle periodogram) of the star computed from the *Kepler* light curve is shown in Fig. 4.

This figure shows five frequency groups (A–E) that are located around 1, 8, 12, 20, and  $40 \mu\text{Hz}$ . We used the Aarhus University extraction of coherent oscillations (ECHO) pipeline (Antoci et al. 2019) to extract the frequencies of these groups. The list of frequencies is given in Table A.1.

Because of the highest amplitude, we may identify group D as Kelvin  $g$ -modes with  $m = 1$  (cf. Paper I). The  $\nu - \sqrt{\Delta\nu}$  diagram given in Fig. 5 demonstrates that the open red circles constructed from the frequencies in group D are generally aligned on a

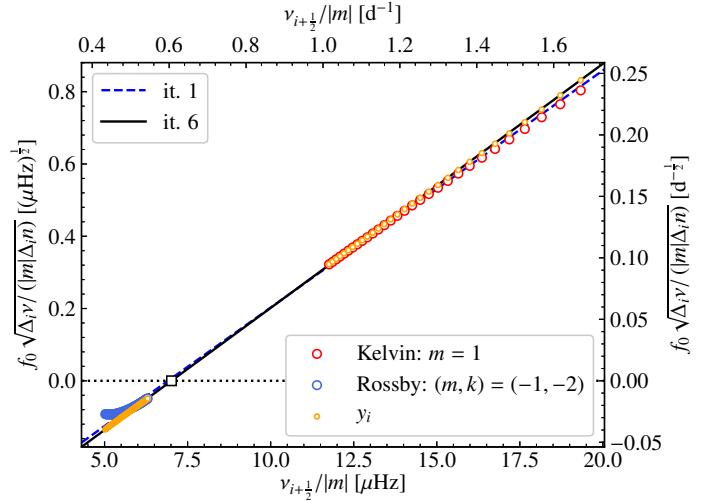


Fig. 3. Same as Fig. 2, but based on both Kelvin and Rossby modes, which are denoted by open red and blue circles, respectively. Small open orange circles represent  $y_i = f_i \sqrt{\Delta_i \nu} / (|m| \Delta_i n)$  that are calculated for the converged value of  $\nu_{\text{rot}}$ .

straight line. However, we also note that these points show small wiggles around the line, which might be interpreted as a signature of the sharp gradient in the chemical composition profiles just outside the convective core (cf. Paper I; Miglio et al. 2008; Kurtz et al. 2014; Saio et al. 2015). Li et al. (2019) pointed out that the same effect is likely to cause the dip in the  $P$ – $\Delta P$  diagram of Rossby modes of this star (see their Fig. 2). We note that most of the frequencies in group D do not have consecutive radial orders, and that  $\Delta_i n$  has to be fixed based on the diagram, as explained in Paper I and indicated by the cyan arrows in the diagram.

We next identify group C with the second highest amplitude as Rossby modes with  $m = -1$  and  $k = -2$ . This is confirmed by the fact that the open blue circles in Fig. 5, which are computed from the frequencies in group C, are roughly found on the same straight line as the open red circles (Kelvin  $g$ -modes).

While group B in Fig. 4 cannot be identified based on the  $\nu - \sqrt{\Delta\nu}$  diagram, its frequency range relative to group C appears to be consistent with that of Rossby modes with  $m = -1$  and  $k = -1$  (Saio et al. 2018). In addition, this group contains some second-order combination frequencies between those in groups C and D (cf. Table A.1). A more detailed analysis is needed to identify modes of these frequencies. We note that even when a detected frequency can be expressed as a linear combination of other frequencies, it can still be an eigenfrequency. This is because it is possible that an eigenmode at the frequency is resonantly excited by the non-linear interaction to have a detectable amplitude. If this is the case, the combination frequency should be treated as a mode frequency in the asteroseismic analysis.

Three of the five frequencies in group E can be explained by the second-order combination frequencies. Their amplitudes of  $\sim 0.1 \text{ mmag}$  are larger by one order of magnitude than the products of the amplitudes of the parent frequencies with amplitudes of a few to several mmag. Although it is difficult to identify the remaining two frequencies, they are located at the expected position for Kelvin  $g$ -modes with  $m = 2$  in the amplitude spectrum.

Many of the low-frequency peaks in group A might not be astrophysical because they are affected by the data analysis of the *Kepler* long-cadence data (e.g. Kurtz et al. 2014). Finally,

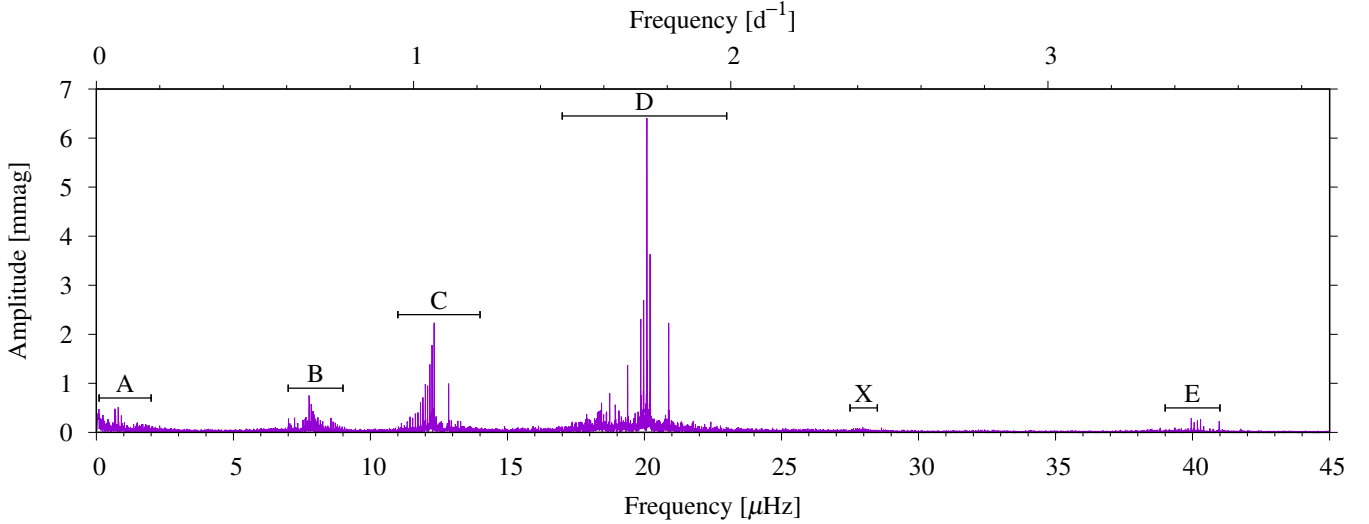


**Fig. 4.** Part of the Lomb-Scargle periodogram of KIC 3240967 computed from the *Kepler* long-cadence data in quarters 1–17 (Q1–Q17). The horizontal bars indicate the ranges of frequency groups A–E. Label X around 28  $\mu\text{Hz}$  indicates the position of non-significant peaks.

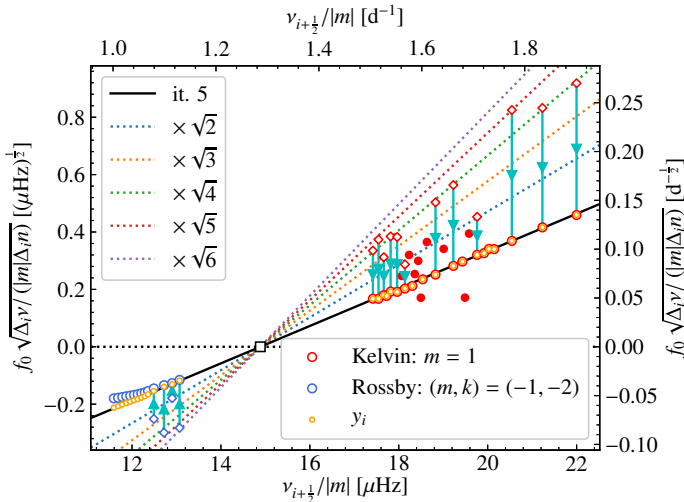


**Fig. 5.** Diagram of  $\nu$  vs.  $\sqrt{\Delta\nu}$  for KIC 3240967. The vertical cyan arrows indicate the identification of  $\Delta_i n$  in the sense that points with an open diamond on the line with “ $\times \sqrt{j}$ ” have  $\Delta_i n = j$ . Open red and blue circles correspond to Kelvin and Rossby modes, respectively, and small open orange circles describe  $y_i = f_i \sqrt{\Delta_i \nu} / (|m| \Delta_i n)$  that are calculated for the converged value of  $\nu_{\text{rot}}$ .

non-significant peaks around 28  $\mu\text{Hz}$ , which are indicated by X in Fig. 4, might be those of Rossby modes with  $m = -2$  and  $k = -2$  (cf. Saio et al. 2018), or combination frequencies.

The results of the iterative linear least-squares fitting based on the frequencies in group D (Kelvin  $g$ -modes with  $m = 1$ ) and/or group C (Rossby modes with  $m = -1$  and  $k = -2$ ) are provided in Table 2. We note that the points with the filled red circles in Fig. 5 were discarded in the fitting because they do not follow the expected behaviour of the Kelvin  $g$ -modes under the traditional approximation of rotation in the asymptotic regime. As discussed in Paper I, they might be affected by the avoided crossings or contamination of other types of modes. We can make qualitatively the same comments as in the case of the evolutionary model in Sect. 3: the analysis based on the Rossby modes alone requires as many as 11 iterations before convergence; this is because the spin parameter of the lowest-frequency mode is about 9, for which  $f_i$  given by Eq. (13) deviates from its

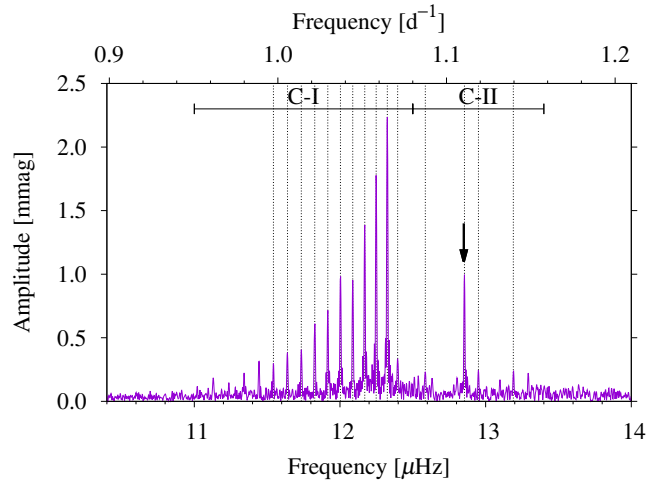


**Fig. 6.** Lomb-Scargle periodogram of KIC 3240967 around frequencies of group C. The vertical dotted lines indicate the extracted frequencies given in Table A.1.

asymptotic value  $f_0$  (cf. Eq. (14)) by 18%; the converged values of  $\nu_{\text{rot}}$  and  $P_0$  based on the Rossby modes alone and those on the Kelvin  $g$ -modes alone more or less agree with each other, although they are not strictly consistent within the given uncertainties; the simultaneous analysis of Kelvin  $g$ - and Rossby modes results in significant reduction of the uncertainties in and the correlation between  $\nu_{\text{rot}}$  and  $P_0$ . Our converged value of  $\nu_{\text{rot}}$  based on both Kelvin  $g$ - and Rossby modes is completely consistent with Li et al. (2019), while that of  $P_0$  ( $4.25 \times 10^3$  s) is larger than their estimate of  $4.18 \times 10^3$  s by 2%. Although we find two peaks in the amplitude spectrum that have consistent frequencies with the estimated  $\nu_{\text{rot}}$  and  $2\nu_{\text{rot}}$  within the uncertainties, they are not statistically significant.

We note the amplitude structure of group C. Figure 6 shows the amplitude spectrum of group C, in which we observe two subgroups, C-I and C-II. Group C-I consists of modes below 12.5  $\mu\text{Hz}$  with consecutive radial orders. In this subgroup, the amplitude of the modes first increases as the frequency is higher. It becomes maximum at 12.3  $\mu\text{Hz}$  and decreases rapidly beyond this frequency. Group C-II is composed of four frequencies

**Table 2.** Same as Table 1, but for KIC 3240967.

	$\nu_{\text{rot}}$ [ $\mu\text{Hz}$ ]	$\nu_{\text{rot}}$ [ $\text{d}^{-1}$ ]	$P_0$ [ $10^3$ s]	$a$	$f_i/f_0$	
					Kelvin	Rossby
Rossby modes with $m = -1$ and $k = -2$ (group C)						
It. 1	15.6(2)	1.35(2)	2.2(3)			
It. 11	14.86(6)	1.284(5)	4.3(2)	−0.995		1.02–1.18
Kelvin $g$ -modes with $m = 1$ (group D)						
It. 1	14.96(6)	1.292(5)	4.35(9)			
It. 3	14.96(6)	1.293(5)	4.37(9)	0.971	0.999–1.001	
Kelvin and Rossby modes (group C and D)						
It. 1	14.76(3)	1.275(3)	4.04(7)			
It. 5	14.887(8)	1.2862(7)	4.25(2)	−0.048	1.000–1.001	1.02–1.18
L19	14.902(9)	1.2857(8)	4.18(2)			

**Reference.** L19: Li et al. (2019).

above  $12.5\mu\text{Hz}$ , which have non-consecutive radial orders. Group C-II shows an isolated high peak of about 1 mmag at  $12.85\mu\text{Hz}$ , which is indicated by an arrow in Fig. 6, while the peaks at the other frequencies are only about 0.2 mmag high. It might appear that the two subgroups originate from different types of modes because the amplitude distribution is clearly different between them. With the assumption of  $m = -1$  and the rotation frequency of  $14.9\mu\text{Hz}$  (cf. Table 2), we may estimate the spin parameters of the frequencies in group C-II to be 12.9 and above, which is consistent with those of Rossby modes with  $k = -3$  (cf. Fig. 1). However, we reject this mode identification of group C-II because we fail to construct the  $\nu - \sqrt{\Delta\nu}$  diagram with  $k = -3$  that shows clear alignment of points on a straight line (or a smooth curve), in sharp contrast to Fig. 5. We thus regard all of the frequencies in group C as those of Rossby modes with  $m = -1$  and  $k = -2$ . Still, we do not understand why the amplitude structure of these modes changes suddenly around  $12.5\mu\text{Hz}$ . If the amplitude is determined by the mode visibility alone, the envelope of the amplitude in group C-I should extend as far as about the rotation frequency of  $14.9\mu\text{Hz}$  (cf. Saio et al. 2018). The reason for the isolated peak at  $12.85\mu\text{Hz}$  also needs to be explained. While we assume that the amplitude is controlled by the physical mechanism of mode excitation and damping, the problem needs to be discussed in more detail in a separate study. We finally note that the similar amplitude distribution of Rossby modes can also be found in other stars, including KIC 3448365 and KIC 9480469, the spectra of which are shown in Fig. A2 of Saio et al. (2018).

#### 4.2. KIC 12066947

We analysed another  $\gamma$  Dor star, KIC 12066947, based on the  $\nu - \sqrt{\Delta\nu}$  diagram. The amplitude spectrum of the star is shown in Fig. 7, and the extracted frequencies are listed in Table A.2. These frequencies were obtained by the method described in Antoci et al. (2019), and are found in five groups, which we refer to as groups U-0, U-1, A, B, and C in the order of frequency. Group B between 26 and  $38\mu\text{Hz}$  consists of Kelvin  $g$ -modes with  $m = 1$ , and has been analysed in Christophe et al. (2018) and Paper I. On the other hand, group A between 19 and  $25\mu\text{Hz}$  can be identified as Rossby modes with  $m = -1$  and  $k = -2$ , as in Van Reeth et al. (2016). We note that in contrast to Christophe et al. (2018), we find the peaks between 56 and  $69\mu\text{Hz}$  (group C) to be statistically significant. This is because

after more detailed analyses, we discovered that using only data from the quarters Q10–Q17, hence removing Q0 and Q1 due to poorer quality, increases the number of extracted frequencies. We identify the frequencies in group C as Kelvin  $g$ -modes with  $m = 2$ . We also observe in Fig. 7 two more groups around 2 and  $10\mu\text{Hz}$ , which are indicated by labels U-0 and U-1, respectively. The former could come from a combination frequencies or artefacts of data analysis, while the latter might originate from Rossby modes with  $m = -1$  and  $k = -1$ . Figure 8 shows the  $\nu - \sqrt{\Delta\nu}$  diagram, and Table 3 provides the estimates of  $\nu_{\text{rot}}$  and  $P_0$ .

We confirm the mode identification of group A based on the  $\nu - \sqrt{\Delta\nu}$  diagram. The main difficulty comes from the non-consecutive radial orders:  $\Delta i/n > 1$  for most cases. The problem can be solved using the results of Paper I based on Kelvin  $g$ -modes. By extending the best-fit line (of Paper I) on the diagram to the lower left side of the abscissa intercept, and drawing other lines with the common intercept and the slopes multiplied by  $\sqrt{2}$ ,  $\sqrt{3}$ ,  $\dots$ , we can verify whether each mode of group A is found on one of these lines. We can verify this when we assume  $m = -1$  and  $k = -2$ , and obtain  $\Delta i/n$  for each point on the diagram, as indicated in Fig. 8. We can similarly verify the identification of group C as Kelvin  $g$ -modes with  $m = 2$ . We note that there are a few exceptional points with filled blue, red, and grey circles in Fig. 8. Because these points have too large  $\Delta i/n$  to be identified reliably or do not align on the straight line that the other points do, we excluded them from the fitting process to estimate  $\nu_{\text{rot}}$  and  $P_0$ .

When we have found  $\Delta i/n$ , we can analyse groups A, B, and C separately. The results based on group A alone (Rossby modes with  $m = -1$  and  $k = -2$ ), group B (Kelvin  $g$ -modes with  $m = 1$ ), and group C (Kelvin  $g$ -modes with  $m = 2$ ) are given in rows 3–5, 6–8, and 9–11 of Table 3, respectively. The converged values of the parameters  $\nu_{\text{rot}}$  and  $P_0$  are consistent within the formal uncertainties in the three cases. Comparing the results for groups A and B, we find that the uncertainties in  $\nu_{\text{rot}}$  are similar ( $\sim 0.3\%$ ), and that the error in  $P_0$  is larger for group A (6%) than for group B (2%). On the other hand, the uncertainties in  $\nu_{\text{rot}}$  and  $P_0$  for group C are larger by about an order of magnitude than those for group B.

The three types of modes can be used simultaneously to obtain the results in rows 12–14 of Table 3. The uncertainties in the two parameters are smaller by a few factors than in the separate analysis of group B. These estimates are completely

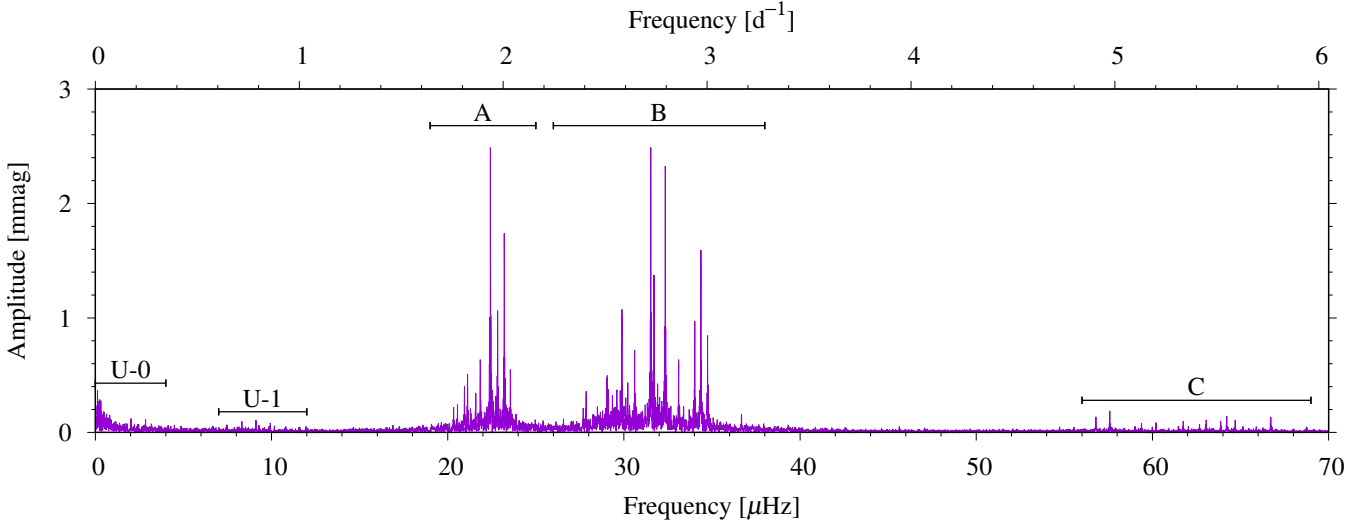


**Fig. 7.** Part of the Lomb-Scargle periodogram of KIC 12066947 computed from the *Kepler* long-cadence data in quarters 10–17 (Q10–Q17). The horizontal bars indicate the ranges of frequency groups.

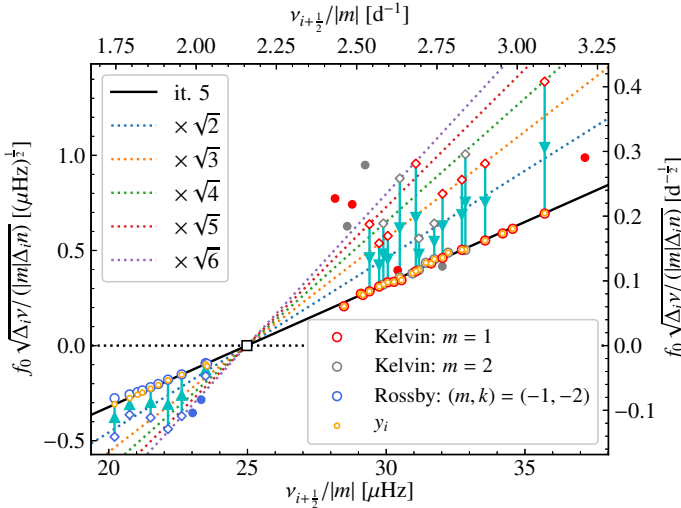


**Fig. 8.** Diagram of  $\nu$  vs.  $\sqrt{\Delta\nu}$  for KIC 12066947 in the same format as Fig. 5.

consistent with those of Li et al. (2019), who considered only the two types, Rossby modes (with  $m = -1$  and  $k = -2$ ) and Kelvin  $g$ -modes with  $m = 1$ . As in the case of Sect. 3.2, the correlation coefficient between the estimated  $\nu_{\text{rot}}$  and  $P_0$  is significantly reduced to 0.56 because different types of modes are used. In addition, the outputs of the first iteration,  $\nu_{\text{rot}} = 24.88 \mu\text{Hz}$  and  $P_0 = 4.07 \times 10^3 \text{ s}$ , are different from the converged values of  $\nu_{\text{rot}} = 24.98 \pm 0.02 \mu\text{Hz}$  and  $P_0 = (4.20 \pm 0.03) \times 10^3 \text{ s}$ , by only 0.4% and 3%, respectively. We note that there is a non-significant peak in the Lomb-Scargle periodogram at the frequency consistent with  $\nu_{\text{rot}} = 24.98 \pm 0.02 \mu\text{Hz}$ .

## 5. Discussion and conclusion

We have extended the method of the  $\nu - \sqrt{\Delta\nu}$  diagram to take not only Kelvin  $g$ -modes, but also Rossby modes with  $k \leq -2$  into account in order to diagnose the internal structure of  $\gamma$  Dor stars from their oscillations. Kelvin and Rossby modes are the most and second most frequently detected modes in  $\gamma$  Dor stars, respectively. The majority of the observed modes are identified

as either one or the other of these modes (e.g. Li et al. 2020). The (average) rotation frequency  $\nu_{\text{rot}}$  and the characteristic period of gravity-mode oscillations  $P_0$  can be estimated by the iterative linear fitting based on the diagram. The extension was made straightforwardly by noting that as in the case of Kelvin  $g$ -modes, the frequencies of Rossby modes with  $k \leq -2$  tend to be independent of  $\nu_{\text{rot}}$  in the co-rotating frame for large  $\nu_{\text{rot}}$ . Rossby modes are located in the region of negative ordinates and lower frequencies than Kelvin  $g$ -modes in the diagram. The rotation frequency  $\nu_{\text{rot}}$  is found between the frequency distributions of the two modes. The estimates of  $\nu_{\text{rot}}$  and  $P_0$  are significantly improved when Kelvin and Rossby modes are used simultaneously in the following two points: (1) reduction of the uncertainties and (2) a lower (anti-)correlation between the estimates. These were confirmed first with a theoretical model in Sect. 3 and then based on two *Kepler* stars, KIC 3240967 and KIC 12066947, in Sect. 4. According to Fig. 13 of Li et al. (2020), the estimated rotation frequency of  $14.887 \pm 0.008 \mu\text{Hz}$  ( $1.2862 \pm 0.0007 \text{ d}^{-1}$ ) of the former is typical for  $\gamma$  Dor stars, while that of the latter of  $24.98 \pm 0.02 \mu\text{Hz}$  ( $2.158 \pm 0.002 \text{ d}^{-1}$ ) is close to the upper end of the distribution.

Eigenmodes of low-frequency oscillations in rotating stars can generally be classified in the traditional approximation of rotation. Each type of modes corresponds to a sequence of eigenvalues of the Laplace tidal equation,  $\lambda$ , which is a function of the spin parameter  $s$  (cf. Fig. 1). The behaviour of Kelvin  $g$ -modes and Rossby modes with  $k \leq -2$  is different from the other types of modes because only these two types have finite  $\lambda$  as  $s$  becomes large, while  $\lambda$  of the other types diverges quadratically ( $\lambda \propto s^2$ ) (e.g. Townsend 2003). Because large  $\lambda$  means short horizontal wavelengths, which lead to significant geometrical cancellation, these types of modes are quite difficult to detect in rapid rotators. The convergence of  $\lambda$  to finite values is a key point for the method of the  $\nu - \sqrt{\Delta\nu}$  diagram because the (quasi-)linear relation of Eq. (10) is derived from this property. It is just fortunate that the problem can be reduced to a linear one only for the modes that are easy to observe.

Although Kelvin and Rossby modes are different in their physical characters and in the observed frequency ranges, they provide almost the same information (particularly about the two structural parameters  $\nu_{\text{rot}}$  and  $P_0$ ) in so far as the degree of differential rotation is weak. This is because their frequencies can



**Table 3.** Same as Table 1, but for KIC 12066947.

	$\nu_{\text{rot}}$ [ $\mu\text{Hz}$ ]	$\nu_{\text{rot}}$ [ $\text{d}^{-1}$ ]	$P_0$ [ $10^3$ s]	$a$	$f_i/f_0$ Kelvin	Rossby
Rossby modes with $m = -1$ and $k = -2$ (group A)						
It. 1	25.5	2.20	2.9			
It. 11	24.96(9)	2.157(8)	4.3(2)	-0.99		1.01–1.15
Kelvin $g$ -modes with $m = 1$ (group B)						
It. 1	24.94	2.155	4.13			
It. 3	24.96(8)	2.156(7)	4.16(9)	0.98	1.000–1.003	
Kelvin $g$ -modes with $m = 2$ (group C)						
It. 1	24.8	2.14	4.0			
It. 3	24.8(7)	2.14(6)	4.0(9)	0.99	1.000–1.003	
Kelvin and Rossby modes (group A–C)						
It. 1	24.88	2.149	4.07			
It. 5	24.98(2)	2.158(2)	4.20(3)	0.56	1.000–1.004	1.01–1.13
L19	24.99(2)	2.159(2)	4.17(3)			

**Reference.** L19: Li et al. (2019).

both be quite accurately explained by Eq. (1) in the traditional approximation of rotation. They differ only in the value of  $\lambda$ . The inner turning points of their propagation cavity are essentially fixed by the outer edge of the convective core, while the outer turning points can weakly depend on the frequency. However, the effect on the integrals in Eqs. (2) and (3) is limited because the dominant contribution comes from the layers just outside the convective core where the Brunt–Väisälä frequency has a high peak. Because the two types of modes give almost the same average of the rotation profile, the possibility of weak differential rotation (in the radial direction) cannot be rejected even though the estimates of  $\nu_{\text{rot}}$  between them in Sect. 4 are consistent with each other. The latitudinal differential rotation can also be studied using the fact that Kelvin and Rossby modes have large amplitudes near the equator and in the mid-latitude region, respectively. More detailed analyses are clearly needed.

While the frequencies of  $\gamma$  Dor stars can mostly be interpreted in the traditional approximation of rotation, the uncertainties in the observed data taken by *Kepler* are so small that in the next step, we need to correct the approximation to fully understand the fine structure of the frequency spectrum (cf. Sect. 3). Another direction of future study is to apply the method to rapidly rotating hybrid pulsators of  $\gamma$  Dor and  $\delta$  Sct type (e.g. Grigahcène et al. 2010). Estimates of  $\nu_{\text{rot}}$  and  $P_0$  from the low-frequency modes will be helpful to understand the spectrum of the high-frequency modes, which is known to be very complicated (e.g. Dziembowski 1990).

**Acknowledgements.** We thank NASA and the *Kepler* team for their revolutionary data. M.T. is partially supported by JSPS KAKENHI Grant Number JP18K03695. S.J.A.J.S. has received funding from the European Research Council (ERC) under the European Union’s Horizon 2020 research and innovation programme (Grant agreement No 833925, project STAREX). This work was supported by a research grant (00028173) from VILLUM FONDEN. Funding for the Stellar Astrophysics Centre is provided by The Danish National Research Foundation (Grant agreement no.: DNRF106).

## References

Antoci, V., Cunha, M. S., Bowman, D. M., et al. 2019, *MNRAS*, **490**, 4040

- Baglin, A., Auvergne, M., Boissard, L., et al. 2006, in *36th COSPAR Scientific Assembly*, COSPAR Meeting, 36
- Ballot, J., Lignières, F., Prat, V., Reese, D. R., & Rieutord, M. 2012, in *Progress in Solar/Stellar Physics with Helio- and Asteroseismology*, eds. H. Shibahashi, M. Takata, & A. E. Lynas-Gray, *ASP Conf. Ser.*, **462**, 389
- Beck, P. G., Bedding, T. R., Mosser, B., et al. 2011, *Science*, **332**, 205
- Beck, P. G., Montalbán, J., Kallinger, T., et al. 2012, *Nature*, **481**, 55
- Bedding, T. R., Huber, D., Stello, D., et al. 2010, *ApJ*, **713**, L176
- Bedding, T. R., Mosser, B., Huber, D., et al. 2011, *Nature*, **471**, 608
- Borucki, W. J., Koch, D., Basri, G., et al. 2010, *Science*, **327**, 977
- Chaplin, W. J., & Miglio, A. 2013, *ARA&A*, **51**, 353
- Christophe, S., Ballot, J., Ouazzani, R.-M., Antoci, V., & Salmon, S. J. A. J. 2018, *A&A*, **618**, A47
- Deheuvels, S., Garcia, R. A., Chaplin, W. J., et al. 2012, *ApJ*, **756**, 19
- Deheuvels, S., Doğan, G., Goupil, M. J., et al. 2014, *A&A*, **564**, A27
- Dziembowski, W. 1990, in *Toward Seismology of  $\delta$  Scuti Stars*, eds. Y. Osaki, & H. Shibahashi, 367, 359
- Eckart, C. 1960, *Hydrodynamics of Oceans and Atmospheres* (New York: Pergamon Press)
- Gill, A. 1982, *Atmosphere-ocean Dynamics* (New York: Academic Press)
- Gough, D. 1985, *Sol. Phys.*, **100**, 65
- Grigahcène, A., Antoci, V., Balona, L., et al. 2010, *ApJ*, **713**, L192
- Kurtz, D. W., Saio, H., Takata, M., et al. 2014, *MNRAS*, **444**, 102
- Lee, U., & Saio, H. 1997, *ApJ*, **491**, 839
- Li, G., Van Reeth, T., Bedding, T. R., Murphy, S. J., & Antoci, V. 2019, *MNRAS*, **487**, 782
- Li, G., Van Reeth, T., Bedding, T. R., et al. 2020, *MNRAS*, **491**, 3586
- Miglio, A., Montalbán, J., Noels, A., & Eggenberger, P. 2008, *MNRAS*, **386**, 1487
- Mosser, B., Barban, C., Montalbán, J., et al. 2011, *A&A*, **532**, A86
- Osaki, Y. 1975, *PASJ*, **27**, 237
- Ouazzani, R.-M., Dupret, M.-A., & Reese, D. R. 2012, *A&A*, **547**, A75
- Ouazzani, R.-M., Roxburgh, I. W., & Dupret, M.-A. 2015, *A&A*, **579**, A116
- Ouazzani, R.-M., Salmon, S. J. A. J., Antoci, V., et al. 2017, *MNRAS*, **465**, 2294
- Papaloizou, J., & Pringle, J. E. 1978, *MNRAS*, **182**, 423
- Ricker, G. R., Winn, J. N., Vanderspek, R., et al. 2014, in *Transiting Exoplanet Survey Satellite (TESS)*, SPIE Conf. Ser., 9143, 914320
- Rossby, C. G. 1939, *J. Mar. Res.*, **2**, 38
- Saio, H. 2018, ArXiv e-prints [arXiv:1812.01253]
- Saio, H., Kurtz, D. W., Takata, M., et al. 2015, *MNRAS*, **447**, 3264
- Saio, H., Kurtz, D. W., Murphy, S. J., Antoci, V. L., & Lee, U. 2018, *MNRAS*, **474**, 2774
- Schmid, V. S., Tkachenko, A., Aerts, C., et al. 2015, *A&A*, **584**, A35
- Takata, M., Ouazzani, R.-M., Saio, H., et al. 2020, *A&A*, **635**, A106
- Thomson, W. 1880, *Proc. R. Soc. Edinburgh*, **10**, 92
- Townsend, R. H. D. 2003, *MNRAS*, **340**, 1020
- Van Reeth, T., Tkachenko, A., Aerts, C., et al. 2015, *ApJS*, **218**, 27
- Van Reeth, T., Tkachenko, A., & Aerts, C. 2016, *A&A*, **593**, A120

## Appendix A: Additional tables

Table A.1. Frequency list of KIC 3240967.

Index	Frequency		Amplitude [mmag]	Group	Combination
	[ $\mu\text{Hz}$ ]	[ $\text{d}^{-1}$ ]			
1	20.08769(2)	1.735576(1)	6.40(3)	D	
2	20.20353(3)	1.745585(3)	3.56(3)	D	
3	19.97140(4)	1.725529(3)	2.93(3)	D	$2\nu_1 - \nu_2$
4	12.32498(2)	1.064878(2)	2.36(1)	C	
5	19.86490(5)	1.716327(5)	2.27(3)	D	
6	20.88416(5)	1.804391(4)	2.23(2)	D	$3\nu_2 - 2\nu_5$
7	12.24898(3)	1.058312(2)	1.89(1)	C	
8	12.16990(4)	1.051479(3)	1.43(1)	C	$-\nu_4 + 2\nu_7$
9	19.3866(1)	1.675002(9)	1.38(3)	D	
10	12.85456(8)	1.110634(7)	1.02(2)	C	
11	12.00333(5)	1.037088(4)	1.00(1)	C	
12	12.08778(5)	1.044385(5)	0.95(1)	C	$2\nu_1 - 2\nu_2 + \nu_4$
13	7.7625(1)	0.67068(1)	0.78(2)	B	$\nu_1 - \nu_4$
14	11.91622(7)	1.029561(6)	0.69(1)	C	$-\nu_2 + \nu_5 + \nu_7$
15	11.82688(8)	1.021843(6)	0.65(1)	C	
16	7.8386(2)	0.67726(1)	0.58(2)	B	$\nu_1 - \nu_7$
17	0.7971(3)	0.06887(3)	0.54(4)	A	$-\nu_1 + 3\nu_2 - 2\nu_5$
18	7.9179(2)	0.68410(2)	0.48(2)	B	$\nu_1 + \nu_4 - 2\nu_7$
19	0.6792(4)	0.05868(3)	0.45(4)	A	$2\nu_2 - 2\nu_5$
20	11.7349(1)	1.013898(9)	0.44(1)	C	
21	7.8787(2)	0.68072(2)	0.43(2)	B	$\nu_2 - \nu_4$
22	18.2827(4)	1.57963(4)	0.42(4)	D	
23	18.3277(4)	1.58352(3)	0.42(4)	D	
24	18.5108(4)	1.59934(4)	0.41(4)	D	
25	19.0690(4)	1.64756(3)	0.41(3)	D	$\nu_1 - 3\nu_2 + 3\nu_5$
26	11.6402(1)	1.00571(1)	0.41(1)	C	$-2\nu_2 + 2\nu_5 + \nu_4$
27	18.3920(4)	1.58907(4)	0.41(4)	D	
28	0.1119(5)	0.00966(4)	0.38(4)	A	$-\nu_1 + \nu_2$
29	17.8907(5)	1.54575(4)	0.38(4)	D	
30	0.9118(5)	0.07878(4)	0.38(4)	A	
31	7.9547(2)	0.68728(2)	0.37(2)	B	$\nu_2 - \nu_7$
32	19.6598(3)	1.69861(3)	0.36(3)	D	
33	12.3963(2)	1.07104(1)	0.36(1)	C	$2\nu_4 - \nu_7$
34	7.6468(3)	0.66068(2)	0.35(2)	B	$2\nu_1 - \nu_2 - \nu_4$
35	0.2383(6)	0.02059(5)	0.32(4)	A	$-2\nu_1 + 2\nu_2$
36	8.0846(3)	0.69851(3)	0.31(2)	B	
37	7.2334(3)	0.62497(3)	0.31(2)	B	
38	18.1803(5)	1.57078(5)	0.31(4)	D	
39	8.5600(3)	0.73959(2)	0.31(2)	B	$3\nu_2 - 2\nu_5 - \nu_4$
40	11.5433(1)	0.99734(1)	0.30(1)	C	$3\nu_2 - \nu_4 - 3\nu_7$
41	7.9995(3)	0.69116(3)	0.30(2)	B	$-\nu_1 + 2\nu_2 - \nu_4$
42	39.9524(2)	3.45189(1)	0.29(1)	E	$\nu_1 + \nu_5$
43	7.0109(4)	0.60574(3)	0.27(2)	B	
44	40.2913(2)	3.48117(1)	0.261(9)	E	$\nu_1 + \nu_2$
45	18.9526(6)	1.63751(5)	0.26(3)	D	
46	7.7220(4)	0.66718(3)	0.26(2)	B	$2\nu_1 - \nu_2 - \nu_7$
47	7.5398(4)	0.65144(3)	0.25(2)	B	$\nu_5 - \nu_4$
48	12.5859(3)	1.08742(2)	0.25(2)	C	$\nu_2 - \nu_5 + \nu_7$
49	7.6161(4)	0.65803(3)	0.25(2)	B	$\nu_5 - \nu_7$

**Notes.** Frequencies are given in the descending order of the amplitude (in Col. 4). In Cols. 2–4, single digits in parentheses represent the errors in the last digits of the preceding numbers. Groups in Col. 5 correspond to those in Fig. 4. In Col. 6,  $\nu_k$  indicates the frequency of index  $k$  (in Col. 1).

Table A.1. continued.

Index	Frequency		Amplitude [mmag]	Group	Combination
	[ $\mu$ Hz]	[d $^{-1}$ ]			
50	8.1716(4)	0.70602(3)	0.24(2)	B	
51	18.0371(7)	1.55840(6)	0.24(4)	D	
52	40.1758(2)	3.47119(2)	0.23(1)	E	$2\nu_1$
53	17.6140(7)	1.52185(6)	0.23(4)	D	
54	13.1903(4)	1.13964(4)	0.22(2)	C	
55	40.9717(2)	3.53996(1)	0.224(8)	E	$\nu_1 + 3\nu_2 - 2\nu_5$
56	17.3621(6)	1.50009(6)	0.22(3)	D	
57	17.7114(7)	1.53026(6)	0.22(4)	D	
58	8.6363(4)	0.74617(3)	0.22(2)	B	$3\nu_2 - 2\nu_5 - \nu_7$
59	40.0591(2)	3.46111(2)	0.22(1)	E	$3\nu_1 - \nu_2$
60	12.9509(4)	1.11896(4)	0.21(2)	C	
61	8.2611(4)	0.71376(4)	0.20(2)	B	
62	1.0208(8)	0.08820(7)	0.20(4)	A	$3\nu_2 - 3\nu_5$
63	22.4201(3)	1.93710(3)	0.20(2)	D	
64	8.0364(5)	0.69435(4)	0.20(2)	B	$\nu_2 + \nu_4 - 2\nu_7$
65	0.2634(9)	0.02276(8)	0.20(4)	A	
66	8.7148(4)	0.75296(3)	0.19(2)	B	
67	18.4816(9)	1.59681(8)	0.19(4)	D	
68	17.4744(8)	1.50979(7)	0.19(4)	D	
69	1.6536(8)	0.14287(7)	0.19(4)	A	
70	18.5662(9)	1.60412(8)	0.19(4)	D	
71	17.7428(9)	1.53298(8)	0.18(4)	D	
72	1.3610(9)	0.11759(8)	0.18(4)	A	
73	1.4975(9)	0.12938(8)	0.18(4)	A	
74	0.361(1)	0.03122(9)	0.18(4)	A	
75	7.0627(5)	0.61022(5)	0.18(2)	B	
76	1.6962(9)	0.14656(8)	0.18(4)	A	
77	8.1164(6)	0.70126(5)	0.16(2)	B	$-2\nu_1 + 3\nu_2 - \nu_4$
78	19.5042(8)	1.68516(7)	0.16(3)	D	
79	1.574(1)	0.13596(9)	0.16(4)	A	
80	18.699(1)	1.61563(9)	0.16(4)	D	
81	8.1994(6)	0.70843(5)	0.16(2)	B	
82	0.647(1)	0.0559(1)	0.15(4)	A	
83	1.814(1)	0.15670(9)	0.15(4)	A	
84	1.888(1)	0.16309(9)	0.15(3)	A	
85	1.804(1)	0.15588(9)	0.15(4)	A	$-3\nu_5 + 2\nu_4 + 3\nu_7$
86	18.098(1)	1.5637(1)	0.15(4)	D	
87	21.5768(6)	1.86424(5)	0.15(2)	D	
88	19.475(1)	1.68263(8)	0.14(3)	D	

**Table A.2.** Frequency list of KIC 12066947.

Index	Frequency		Amplitude [mmag]	Group	Combination
	[ $\mu\text{Hz}$ ]	[ $\text{d}^{-1}$ ]			
1	31.52523(4)	2.723780(3)	2.57(1)	B	
2	22.42210(3)	1.937270(3)	2.543(9)	A	
3	32.34838(3)	2.794900(3)	2.382(9)	B	
4	23.20935(5)	2.005288(5)	1.73(1)	A	
5	34.37169(4)	2.969714(4)	1.579(7)	B	
6	31.71175(6)	2.739895(5)	1.43(1)	B	
7	22.83400(8)	1.972858(7)	1.13(1)	A	
8	29.8904(1)	2.58253(1)	1.10(1)	B	
9	34.02411(7)	2.939683(6)	0.986(7)	B	
10	34.74867(7)	3.002285(6)	0.875(7)	B	$2\nu_1 - 3\nu_3 + 2\nu_5$
11	30.6102(1)	2.64472(1)	0.79(1)	B	$-3\nu_1 + \nu_3 + 4\nu_4$
12	21.8456(1)	1.887458(9)	0.638(7)	A	
13	23.5559(2)	2.03523(1)	0.59(1)	A	
14	33.1085(1)	2.86058(1)	0.587(8)	B	
15	21.1275(1)	1.82542(1)	0.478(6)	A	
16	29.0494(3)	2.50987(3)	0.47(2)	B	$4\nu_1 - 3\nu_3$
17	30.2228(3)	2.61125(2)	0.46(1)	B	
18	29.1235(4)	2.51627(3)	0.40(2)	B	$-\nu_1 + 4\nu_3 - 2\nu_5$
19	27.8576(4)	2.40690(3)	0.40(1)	B	$3\nu_1 - \nu_3 - \nu_5$
20	29.6013(3)	2.55755(3)	0.40(1)	B	
21	20.9484(1)	1.80994(1)	0.391(6)	A	$4\nu_2 - 2\nu_5$
22	21.2936(2)	1.83977(2)	0.236(6)	A	
23	20.5530(2)	1.77578(2)	0.223(6)	A	
24	30.3352(6)	2.62096(5)	0.22(1)	B	
25	28.4983(7)	2.46226(6)	0.22(2)	B	$\nu_2 - 3\nu_3 + 3\nu_5$
26	57.5803(3)	4.97494(3)	0.189(7)	C	$\nu_4 + \nu_5$
27	30.4919(6)	2.63450(5)	0.19(1)	B	
28	21.7233(4)	1.87689(3)	0.175(7)	A	
29	64.2208(3)	5.54868(3)	0.158(5)	C	
30	0.639(1)	0.0552(1)	0.15(2)	U-0	
31	36.6750(4)	3.16872(3)	0.142(6)	B	
32	56.7933(5)	4.90694(4)	0.141(7)	C	$\nu_2 + \nu_5$
33	28.456(1)	2.4586(1)	0.14(2)	B	
34	0.033(1)	0.0029(1)	0.14(2)	U-0	
35	66.7198(3)	5.76459(3)	0.132(5)	C	$\nu_3 + \nu_5$
36	63.0506(4)	5.44757(4)	0.116(5)	C	$2\nu_1$
37	64.6977(5)	5.58988(4)	0.115(6)	C	$2\nu_3$
38	63.8741(4)	5.51872(4)	0.112(5)	C	$\nu_1 + \nu_3$
39	2.850(1)	0.2462(1)	0.11(2)	U-0	$-\nu_1 + \nu_5$
40	23.5283(9)	2.03285(8)	0.11(1)	A	
41	9.1033(8)	0.78653(7)	0.105(9)	U-1	$\nu_1 - \nu_2$
42	2.026(2)	0.1750(1)	0.10(2)	U-0	$-\nu_3 + \nu_5$
43	61.7496(5)	5.33516(4)	0.101(6)	C	
44	8.3154(9)	0.71845(8)	0.096(9)	U-1	$\nu_1 - \nu_4$
45	9.1398(9)	0.78968(8)	0.089(9)	U-1	$\nu_3 - \nu_4$
46	60.2057(6)	5.20177(5)	0.086(6)	C	$3\nu_1 - \nu_5$
47	29.194(2)	2.5224(2)	0.09(2)	B	$4\nu_2 + \nu_3 - 4\nu_4$
48	59.3816(7)	5.13057(6)	0.084(6)	C	$4\nu_1 - \nu_3 - \nu_5$
49	1.139(2)	0.0984(2)	0.08(2)	U-0	$-\nu_3 - 3\nu_4 + 3\nu_5$
50	23.452(1)	2.0263(1)	0.07(1)	A	
51	9.289(1)	0.8026(1)	0.070(8)	U-1	
52	62.6720(8)	5.41486(7)	0.065(5)	C	$3\nu_3 - \nu_5$
53	19.8642(7)	1.71627(6)	0.065(5)	A	
54	62.0381(8)	5.36009(7)	0.062(6)	C	
55	37.6512(7)	3.25306(6)	0.061(5)	B	

**Notes.** Frequencies are given in the descending order of the amplitude (in Col. 4). In Cols. 2–4, single digits in parentheses represent the errors in the last digits of the preceding numbers. Groups in Col. 5 correspond to those in Fig. 7. In Col. 6,  $\nu_k$  indicates the frequency of index  $k$  (in Col. 1).